remote sensing

MDPI

Article

Mainlobe Coherent Source 3D Imaging via Monopulse Ratio-Based Spatial Steering Vector and Polarization Diversity

Jiahao Tian, Jianxiong Zhou *, Zhanling Wang, Xiangting Wang, Fulai Wang, Zhiyong Song and Ping Wang

College of Electronic Science and Technology, National University of Defense Technology, Changsha 410073, China; tianjiahao@nudt.edu.cn (J.T.); wangzhanling17@nudt.edu.cn (Z.W.); wangxiangting@nudt.edu.cn (X.W.); wangfulai12@nudt.edu.cn (F.W.); songzhiyong08@nudt.edu.cn (Z.S.); wangping@nudt.edu.cn (P.W.)
* Correspondence: jxzhou@nudt.edu.cn or zjxjanet@sina.com

Highlights

What are the main findings?

- A Robust Single-Snapshot 3D Imaging Framework for Coherent Sources: The study establishes a novel projection-feedback mechanism that leverages polarization-angle coupling to achieve accurate 3D localization of mainlobe coherent targets using only a single snapshot. This approach effectively overcomes the performance degradation and data rank deficiency typical of traditional monopulse radar systems under adverse conditions, such as significant target energy disparities.
- Significant Efficiency Gains via Dimensionality Reduction: By exploiting the inherent coupling between signal polarization and spatial steering vectors, the research successfully transforms the complex, multi-parameter angular search space into a computationally efficient 1D line search. This allows for high-precision dual-target resolution with substantially reduced computational overhead compared to conventional super-resolution algorithms.

What are the implications of the main findings?

- Enhanced Operational Capability in High-Dynamic Scenarios: The method provides a low-complexity, real-time alternative to traditional SAR systems, particularly for tracking fast-maneuvering targets. Its reliance on a single snapshot ensures high estimation fidelity even when short-term observations or rapid maneuvers preclude the use of traditional coherent integration or Doppler processing gains.
- Mitigation of Technical Bottlenecks in Complex Environments: By effectively resolving mainlobe coherent sources—a long-standing challenge in radar signal processing—this framework enhances radar reliability in environments prone to multipath interference and coherent jamming. It establishes a theoretical foundation for advancing multi-target super-resolution and 3D remote sensing in increasingly congested and complex surveillance contexts.

Abstract

Traditional angle estimation for sum-and-difference monopulse radar systems is predominantly designed for non-coherent sources or relies on fixed closed-form solutions. However, in the presence of coherent sources, these methods often suffer from performance degradation due to data rank deficiency or unavoidable suppression of target power. To address these limitations, this paper presents a single-snapshot angle estimation method for coherent sources by leveraging the angular super-resolution and ranging capabilities of monopulse radar to achieve 3D imaging in the range-angle domain. The approach utilizes the monopulse ratio spatial steering vector as a search vector and projects the received data

Check for updates

Academic Editor: Riccardo Roncella

Received: 29 March 2026
Revised: 25 April 2026
Accepted: 25 April 2026
Published: 29 April 2026

Copyright: © 2026 by the authors. Licensee MDPI, Basel, Switzerland. This article is an open access article distributed under the terms and conditions of the Creative Commons Attribution (CC BY) license.

onto its orthogonal subspace. By exploiting the coupling characteristics between signal polarization and angle, a cost function is constructed to validate the feedback of the search vector. Theoretical analysis demonstrates that for dual-target scenarios, the cost function reaches its minimum precisely when the search vector aligns with a target's steering vector, enabling the accurate estimation of both targets' angles. Furthermore, the polarization-angle coupling constraint reduces the 2D angular search space to a 1D line, significantly lowering computational complexity. Simulation results indicate that the method effectively resolves dual targets under single-snapshot conditions and maintains robust performance even with significant energy disparities. Finally, 3D localization of multiple airborne point targets is achieved by integrating 2D angular information with range data, validating the potential of the method for advanced radar imaging and positioning.

Keywords: coherent source; monopulse ratio; 3D imaging; single-snapshot; angle estimation; polarization-angle coupling

1. Introduction

Current radar remote sensing is predominantly based on Synthetic Aperture Radar (SAR), which utilizes platform motion to synthesize a virtual large aperture [1] for high-resolution 2D imaging. This technology is widely deployed in monitoring [2] and reconnaissance [3–5]. However, due to the inherent constraints between synthetic aperture size and integration time, a trade-off is often required between imaging duration and precision. Furthermore, coherent integration across the entire scene imposes a significant computational burden. In security monitoring scenarios involving sparse airborne targets—which can be pre-separated via Doppler processing—fine-grained imaging of the entire field of view (FOV) is often unnecessary; instead, coarse imaging or 3D localization suffices. Theoretically, precise target positioning can be achieved by leveraging the angular super-resolution of monopulse radar [6,7] and the ranging capabilities of pulse compression. Particularly in scenarios with moderate resolution requirements, providing simple angle and range information serves as an economical remote sensing alternative. Moreover, monopulse radar is characterized by ease of deployment and immunity to phase fluctuations caused by non-ideal platform motion, making it an attractive approach for low-resolution remote sensing.

Angular resolution is a pivotal metric for evaluating radar performance, determined not only by the physical aperture but also by the efficacy of signal processing algorithms [8]. With the expanding application of radar in military reconnaissance, civil remote sensing, and autonomous driving, electromagnetic environments are becoming increasingly complex, necessitating higher angular estimation accuracy and resolution. Particularly in the presence of interference or dense multi-target scenarios, traditional methods often fail to estimate coherent sources effectively due to the rank deficiency of the covariance matrix [9], thereby limiting the broad application of angle-range-based 3D localization. This underscores a fundamental distinction between the proposed framework and existing remote sensing techniques: while the latter inherently exploits the coherence of echoes from different scattering points to extract relative spatial information, the coherence between multiple target echoes in the proposed framework constitutes an adverse effect that must be rigorously overcome.

The 3D imaging of standard sum-and-difference monopulse radar relies on precise angle estimation. For mainlobe multi-target scenarios, traditional angle estimation follows two primary technical routes. The first route constructs a deterministic-stochastic signal

model linking angular parameters and observations based on specific echo probability distributions, utilizing Maximum Likelihood (ML) [10,11] or the Method of Moments (MOM) [12] to achieve dual-source estimation. While theoretically rigorous, these methods are primarily restricted to non-coherent sources with predefined amplitude statistics; furthermore, significant performance degradation occurs when a substantial power disparity exists between the sources. The second route employs angular super-resolution techniques such as spatial spectrum estimation [13,14] or Compressive Sensing (CS)-based sparse reconstruction [15–17]. The former necessitates large-scale antenna arrays and requires translational invariance of subarray phase centers to implement spatial smoothing for coherent sources [18,19]. The latter, although applicable to arbitrary array configurations, demands high Signal-to-Noise Ratios (SNRs) and a large number of array elements to ensure reconstruction accuracy [20], alongside high computational complexity. Consequently, neither route directly satisfies the requirements for coherent source angle estimation in four-channel monopulse radars.

To mitigate multi-target interference, several separation strategies have been proposed. Increasing range resolution separates scattering centers but fails for targets at identical ranges [8]. Spatial nulling and beamforming techniques [21–23] are limited by angular overlap, where shared azimuth or elevation angles lead to total signal suppression. Pre-processing methods (e.g., eigen-projection or blocking matrices) and Blind Source Separation (BSS) require either unrealistic pure single-target snapshots or source independence, making them inapplicable to coherent mainlobe scenarios [24–29]. Furthermore, the high similarity of steering vectors within the mainlobe causes these schemes to inevitably suppress the target of interest.

Recent studies [7,8] have integrated polarization information into angle estimation, primarily utilizing polarization nulling to suppress one target and estimate the angle of the other. The rank of the Hankel matrix and the determinant of the four-channel echo matrix are typically employed to determine if complete cancellation is achieved. However, the reliability of these methods significantly diminishes when targets exhibit high polarization similarity. Furthermore, Literature [30] utilizes polarization state fluctuations as auxiliary information for angular nulling. Notably, when two sources are coherent, the echoes in both polarization and angular domains exhibit characteristics similar to those of a single target. Consequently, metrics based on rank analysis or polarization fluctuations fail to reflect the true number of targets. Moreover, these methods require multiple snapshots, which deviates from the concept of "monopulse" processing in its strictest sense.

Existing monopulse angle estimation techniques struggle with mainlobe coherent sources. To address this, we propose a single-snapshot projection-feedback method leveraging polarization-angle disparities. This approach enables robust 3D imaging under varying polarization and phase conditions, with high extensibility to non-coherent and general array radar scenarios. The core technical contributions are:

1. Single-Snapshot Coherent 3D Imaging Framework: We establish a flexible, low-complexity imaging framework that serves as an economical complement to traditional SAR systems, requiring only a single sample for execution.
2. Polarization-Angle Coupled Verification: A verification mechanism for monopulse ratio search vectors is developed. It facilitates dual-target resolution in a single snapshot and is applicable to various multi-channel polarized radar architectures.
3. Search Space Reduction Strategy: By exploiting the dual-target echo model, we transform the four-parameter angular search into a 1D search, substantially reducing the computational overhead.

4. Performance Validation: Extensive simulations demonstrate that the proposed method provides superior angular resolution and robustness compared to state-of-the-art approaches.

The remainder of this manuscript is organized as follows. Section 2 presents the system architecture and echo signal model for a dual-polarization four-channel sum-and-difference monopulse radar. Section 3 elaborates on the effectiveness of the proposed feedback verification cost function. Subsequently, Section 4 evaluates the robustness and precision of the algorithm through comprehensive numerical simulations under various parameter configurations. Finally, Section 5 concludes the study by summarizing the primary technical contributions and key findings.

2. Signal Model

Assuming that the radar operates under far-field and narrowband conditions, the geometric scenario for aerial target localization is illustrated in Figure 1. The antenna array of the dual-polarized monopulse radar is partitioned into four symmetric channels: A, B, C, and D. Taking channel A as the phase reference, the echoes from a single point target across the four channels can be expressed as:

$$A = a \cdot e^{j0}, \quad B = a \cdot e^{j\phi_{az}}, \quad C = a \cdot e^{j\phi_{el}}, \quad D = a \cdot e^{j(\phi_{az}+\phi_{el})} \tag{1}$$

where ϕ_{az} and ϕ_{el} denote the inter-channel phase differences determined by the target's azimuth and elevation angles, along with the spacing between the phase centers of the four channels. The term a represents the complex envelope of the echo received by each subarray. Furthermore, the data can be reorganized into sum and difference (Σ & Δ) channels as follows:

$$\begin{cases} \Sigma = A + B + C + D \\ \Delta_{el} = (A + B) - (C + D) \\ \Delta_{az} = (A + C) - (B + D) \\ \Delta\Delta = (A + D) - (B + C) \end{cases} \tag{2}$$

where $\Delta\Delta$ represents the double-difference channel. An explicit proportional relationship exists between the sum and difference channels [31]. Specifically, based on the relationship between path difference and phase difference, the ratio of the elevation difference channel to the sum channel is given by:

$$\frac{\Delta_{el}}{\Sigma} = \frac{(1 - e^{j\phi_{el}})}{(1 + e^{j\phi_{el}})} = -j \tan\left(\frac{\phi_{el}}{2}\right) = -j \tan\left(2\pi \frac{d_e \sin(\varphi) - d_e \sin(\varphi_0)}{2\lambda}\right) \tag{3}$$

where φ_0 is the elevation boresight (steering direction) of the mainlobe, φ is the target's elevation angle, d_e is the phase center spacing between subarrays A and C (or B and D), and λ is the wavelength corresponding to the carrier frequency. For a square antenna array uniformly divided into four subarrays, the spacing d_e is defined as:

$$d_e = \frac{\lambda N_e}{4} \tag{4}$$

where N_e is the number of elements along each dimension of the square array. By applying the small-angle approximation to the trigonometric functions, Equation (3) can be simplified as follows:

$$\frac{\Delta_{el}}{\Sigma} \approx -j\pi N_e \frac{\varphi - \varphi_0}{4} = -jk_{el}\Delta\varphi = -j\eta \tag{5}$$

here, η is defined as the elevation monopulse ratio, and $k_{el} = \pi N_e/4$ is the monopulse slope [32] in the elevation dimension. Equation (5) demonstrates a linear relationship between the monopulse ratio and the angular deviation of the target from the beam boresight. Given its dimensionless property, the monopulse ratio decouples the algorithm's intrinsic capability from specific radar hardware parameters (such as array geometry and beamwidth), ensuring universal applicability across different radar systems. In the subsequent analysis, we focus on the estimation performance of the target's monopulse ratio.

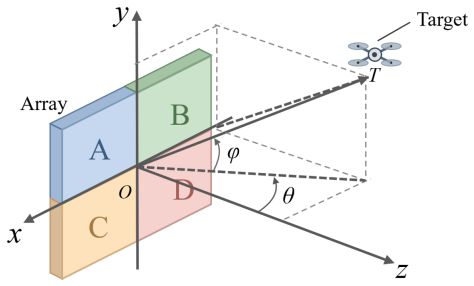

Figure 1. Geometric scenario for aerial target localization.

Similarly, the ratio of the azimuth difference channel to the sum channel can be expressed as:

$$\frac{\Delta_{az}}{\Sigma} \approx -j\pi N_a \frac{\theta - \theta_0}{4} = -jk_{az}\Delta\theta = -j\kappa \tag{6}$$

where κ is defined as the azimuth monopulse ratio, θ is the target's azimuth angle, and $\Delta\theta$ is the angular offset relative to the beam center in azimuth. For the double-difference channel, the ratio is formulated as:

$$\frac{\Delta\Delta}{\Sigma} = \frac{(1 - e^{j\phi_{el}})}{(1 + e^{j\phi_{el}})} \cdot \frac{(1 - e^{j\phi_{az}})}{(1 + e^{j\phi_{az}})} \approx -j\eta \cdot (-j)\kappa = -\eta \cdot \kappa \tag{7}$$

Consequently, the monopulse ratio steering vector for a four-channel radar can be defined as:

$$\boldsymbol{p}_i = [1, -j\eta_i, -j\kappa_i, -\eta_i\kappa_i]^T, \quad i = 1, 2 \tag{8}$$

For array receivers with dual-polarization capabilities, the polarization characteristics of the target—representing the orientation and phase relationship of the electric field vector—can be characterized by the Jones vector:

$$\boldsymbol{h}_i = \begin{bmatrix} \cos\xi_i & \sin\xi_i \cdot e^{j\psi_i} \end{bmatrix}^T \tag{9}$$

where ξ_i represents the polarization auxiliary angle and ψ_i is the polarization phase difference of the i-th target. Finally, taking the effect of noise into account, the joint spatial-polarization sampling matrix for the dual-target echoes can be derived as:

$$\mathbf{X} = a_1\boldsymbol{p}_1\boldsymbol{h}_1^T + a_2\boldsymbol{p}_2\boldsymbol{h}_2^T + \boldsymbol{n} \tag{10}$$

where $\boldsymbol{n}$ is the noise vector following a zero-mean complex Gaussian distribution, denoted as $n \sim \mathcal{CN}(\mathbf{0}, \sigma_n^2\mathbf{I})$. Accordingly, the power ratio γ between the two targets and the SNR are defined as:

$$\gamma = \frac{E(|a_1|^2)}{E(|a_2|^2)}, \quad SNR = \frac{E(|a_2|^2)}{E(\sigma_n^2)} \tag{11}$$

3. Proposed Method

Based on the aforementioned analysis, the joint spatial-polarization sampling matrix of the dual-target echoes is essentially a linear superposition of two rank-one matrices. Consequently, it is theoretically feasible to estimate the parameters of one source by suppressing the other. The fundamental challenge, however, lies in the fact that for two sources with fully coherent waveforms, it is conventionally impossible to determine whether one source has been perfectly suppressed (i.e., leaving only the component of the other) under single-snapshot conditions without any a priori information regarding angle or polarization. This difficulty persists even if multiple sampling matrices are acquired over the time dimension.

Given that a suitable orthogonal projection can completely nullify one source, we utilize the target's spatial steering vector as a search vector to construct an orthogonal projection matrix. A cost function is then developed based on a two-step projection transformation—comprising spatial orthogonal projection and polarization oblique projection—to validate the correctness of the search vector. To intuitively demonstrate the effectiveness of the proposed method, we first analyze the behavior of the cost function under correct search conditions, then generalize the analysis to evaluate its overall effectiveness across broader scenarios.

3.1. Analysis of the Correct Search Vector Scenario

By utilizing the spatial steering vector $\boldsymbol{p}_0$ as a search vector, an orthogonal projection matrix can be constructed as:

$$\mathbf{P}_{\perp}(\eta,\kappa) = \mathbf{I}_4 - \frac{\boldsymbol{p}_0 {\boldsymbol{p}_0}^H}{{\boldsymbol{p}_0}^H \boldsymbol{p}_0} \tag{12}$$

where $\mathbf{I}_4$ is the 4×4 identity matrix, $\boldsymbol{p}_0 = [1, -j\eta, -j\kappa, -\eta\kappa]^T$, and (η, κ) represent the candidate 2D monopulse ratio parameters for the search. Neglecting the effect of noise, the joint spatial-polarization sampling matrix after projection is given by:

$$\mathbf{X}_{\mathrm{p}} = \mathbf{P}_{\perp}\mathbf{X} = a_1 \mathbf{P}_{\perp}\boldsymbol{p}_1 {\boldsymbol{h}_1}^T + a_2 \mathbf{P}_{\perp}\boldsymbol{p}_2 {\boldsymbol{h}_2}^T \tag{13}$$

Based on the properties of orthogonal projection, when the search vector aligns with the first target ($\boldsymbol{p}_0 = \boldsymbol{p}_1$), the first term is nulled, leaving only the information corresponding to the second source:

$$\mathbf{X}_{\mathrm{p}} = a_2 \mathbf{P}_{\perp}\boldsymbol{p}_2 {\boldsymbol{h}_2}^T \tag{14}$$

At this stage, the polarization state of the second target can be estimated using the data from the sum channel:

$$\hat{\boldsymbol{h}}^T = \frac{\mathbf{X}_{\mathrm{p}}(1,:)}{||\mathbf{X}_{\mathrm{p}}(1,:)||} = \boldsymbol{h}_2^T \tag{15}$$

Following the notational convention, $\mathbf{X}_{\mathrm{p}}(i,j)$ denotes the element at the i-th row and j-th column of matrix $\mathbf{X}_{\mathrm{p}}$, and the colon ':' represents the selection of all elements in the respective row or column.

Before formulating the operator, it is essential to clarify the physical rationale of oblique projection in this context. Unlike standard orthogonal projection, the oblique projection acts as a highly selective polarization filter. Specifically, once the polarization direction of the interference ($\hat{h}$) is estimated, this operator projects the data onto a chosen reference subspace (h_0) to seamlessly extract the desired target component while strictly nullifying the associated interference energy, even when their polarization vectors are

non-orthogonal. Subsequently, using the estimated Jones vector $\hat{\boldsymbol{h}}$ and an arbitrary Jones vector $\boldsymbol{h}_0$, an oblique projection matrix can be constructed as:

$$\mathbf{P}_{\boldsymbol{h}_0|\hat{\boldsymbol{h}}} = \boldsymbol{h}_0\left(\boldsymbol{h}_0^H\mathbf{P}_{\hat{\boldsymbol{h}}}\boldsymbol{h}_0\right)^{-1}\boldsymbol{h}_0^H\mathbf{P}_{\hat{\boldsymbol{h}}} \tag{16}$$

where $\mathbf{P}_{\hat{\boldsymbol{h}}} = \mathbf{I}_2 - \hat{\boldsymbol{h}}(\hat{\boldsymbol{h}}^H\hat{\boldsymbol{h}})^{-1}\hat{\boldsymbol{h}}^H$. Here, $\hat{\boldsymbol{h}} = \boldsymbol{h}_2$ represents the steering vector component to be suppressed by the oblique projection. According to the properties of the oblique projection matrix:

$$\begin{aligned}\mathbf{P}_{\boldsymbol{h}_0|\hat{\boldsymbol{h}}}\hat{\boldsymbol{h}} &= \mathbf{0}\\ \mathbf{P}_{\boldsymbol{h}_0|\hat{\boldsymbol{h}}}\boldsymbol{h}_0 &= \boldsymbol{h}_0\end{aligned} \tag{17}$$

Processing the joint spatial-polarization sampling matrix of the mixed echoes with the constructed oblique projection matrix yields:

$$\mathbf{Y} = \mathbf{P}_{\boldsymbol{h}_0|\hat{\boldsymbol{h}}}\mathbf{X}^T = \mathbf{P}_{\boldsymbol{h}_0|\hat{\boldsymbol{h}}}\left(a_1\boldsymbol{h}_1\boldsymbol{p}_1{}^T + a_2\boldsymbol{h}_2\boldsymbol{p}_2{}^T\right) = a_1\mathbf{P}_{\boldsymbol{h}_0|\hat{\boldsymbol{h}}}\boldsymbol{h}_1\boldsymbol{p}_1{}^T \tag{18}$$

For ease of analysis, it is initially assumed that the Jones vectors $\boldsymbol{h}_0$, $\boldsymbol{h}_1$, and $\boldsymbol{h}_2$ are all two-dimensional real vectors; the more general case of complex vectors will be addressed subsequently. Under this assumption, the oblique projection operation is equivalent to a parallelogram decomposition of the vector under operation, as illustrated in Figure 2.

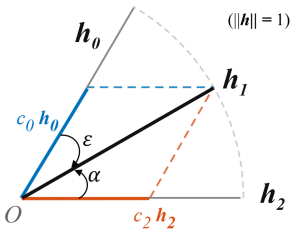

Figure 2. Geometric interpretation of the oblique projection decomposition.

This geometric decomposition explicitly visualizes how the oblique projection isolates the desired component while nulling the interference along its original direction. By applying the Law of Sines to the geometry in Figure 2, it follows that:

$$\mathbf{P}_{\boldsymbol{h}_0|\boldsymbol{h}_2}\boldsymbol{h}_1 = c_0\boldsymbol{h}_0 = \frac{\sin\alpha}{\sin(\alpha-\varepsilon)}\boldsymbol{h}_0 \tag{19}$$

where α is the angular separation from Jones vector $\boldsymbol{h}_2$ to $\boldsymbol{h}_1$, and ε is the angle between $\boldsymbol{h}_0$ and $\boldsymbol{h}_1$. The counter-clockwise direction is defined as the positive angular direction. Consequently, the processed matrix $\mathbf{Y}$ can be expressed as:

$$\mathbf{Y} = \frac{a_1\sin\alpha}{\sin(\alpha-\varepsilon)}\boldsymbol{h}_0\boldsymbol{p}_1^T \tag{20}$$

Considering the initial assumption that $\boldsymbol{p}_0 = \boldsymbol{p}_1$, it follows that each row of the resulting output matrix $\mathbf{Y}$ is aligned to the search vector $\boldsymbol{p}_0{}^T$ used to construct the orthogonal projection matrix. That is:

$$\left\|\frac{\mathbf{Y}(k,:)}{\mathbf{Y}(k,1)} - \boldsymbol{p}_0^T\right\| = 0 \tag{21}$$

where $k = 1$ or 2. Analogously, when $\boldsymbol{p}_0 = \boldsymbol{p}_2$, each row of the output matrix will similarly be aligned to $\boldsymbol{p}_0$, thereby satisfying Equation (21).

Evidently, Equation (21) establishes a feedback verification mechanism for the spatial search vector $\boldsymbol{p}_0$. When $\boldsymbol{p}_0$ aligns with the spatial steering vector of either source in the

mixed echo, the output of the two-step projection transformation satisfies this criterion. Consequently, accurate estimates of the target's monopulse ratios can be obtained, and the corresponding angle estimates are subsequently derived using Equations (5) and (6).

3.2. Analysis of the General Case

In the preceding section, real-valued polarization vectors were utilized as examples to intuitively demonstrate the validity of the cost function under correct search conditions. We now extend this analysis to the general scenario, where the spatial search vector is not aligned to the true steering vectors of either source, and the polarization vectors are considered in the complex domain. In this case, Equation (13) is reformulated as:

$$\begin{aligned} \mathbf{X}_{\mathrm{p}} &= \mathbf{P}_{\perp}\mathbf{X} = a_1\mathbf{P}_{\perp}\boldsymbol{p}_1{\boldsymbol{h}_1}^T + a_2\mathbf{P}_{\perp}\boldsymbol{p}_2{\boldsymbol{h}_2}^T \\ &= \beta_1\boldsymbol{g}_1{\boldsymbol{h}_1}^T + \beta_2\boldsymbol{g}_2{\boldsymbol{h}_2}^T \end{aligned} \tag{22}$$

where $\boldsymbol{g}_1$ and $\boldsymbol{g}_2$ represent the projections of the true steering vectors $\boldsymbol{p}_1$ and $\boldsymbol{p}_2$ into the orthogonal subspace of the search vector $\boldsymbol{p}_0$, respectively. These vectors are normalized such that their first elements equal unity. The coefficients β_1 and β_2 represent the relative amplitude and phase relationships of the directional components. The estimated Jones vector derived from Equation (22) is given by:

$$\hat{\boldsymbol{h}}^{\prime T} = \frac{\mathbf{X}_{\mathrm{p}}(1,:)}{\left|\left|\mathbf{X}_{\mathrm{p}}(1,:)\right|\right|} = \frac{\beta_1{\boldsymbol{h}_1}^T + \beta_2{\boldsymbol{h}_2}^T}{\left|\left|\beta_1{\boldsymbol{h}_1}^T + \beta_2{\boldsymbol{h}_2}^T\right|\right|} \tag{23}$$

This estimate constitutes a weighted sum of the true received Jones vectors of the two sources. Provided that $\boldsymbol{h}_1$ and $\boldsymbol{h}_2$ are not aligned, the composite estimate $\hat{\boldsymbol{h}}^{\prime}$ will not be aligned to either individual Jones vector. Based on Equation (16), the oblique projection matrix can then be constructed using $\hat{\boldsymbol{h}}^{\prime}$ and an arbitrary Jones vector $\boldsymbol{h}_0$:

$$\mathbf{P}_{\boldsymbol{h}_0|\hat{\boldsymbol{h}}^{\prime}} = \boldsymbol{h}_0\left(\boldsymbol{h}_0^H\mathbf{P}_{\hat{\boldsymbol{h}}^{\prime}}\boldsymbol{h}_0\right)^{-1}\boldsymbol{h}_0^H\mathbf{P}_{\hat{\boldsymbol{h}}^{\prime}} \tag{24}$$

The resulting output of the oblique projection is expressed as:

$$\mathbf{Y}^{\prime} = \mathbf{P}_{\boldsymbol{h}_0|\hat{\boldsymbol{h}}^{\prime}}\mathbf{X}^T = \mathbf{P}_{\boldsymbol{h}_0|\hat{\boldsymbol{h}}^{\prime}}a_1\boldsymbol{h}_1{\boldsymbol{p}_1}^T + \mathbf{P}_{\boldsymbol{h}_0|\hat{\boldsymbol{h}}^{\prime}}a_2\boldsymbol{h}_2{\boldsymbol{p}_2}^T \tag{25}$$

Defining $\mathbf{P}_{\boldsymbol{h}_0|\hat{\boldsymbol{h}}^{\prime}}\boldsymbol{h}_1 = c_1\boldsymbol{h}_0$ and $\mathbf{P}_{\boldsymbol{h}_0|\hat{\boldsymbol{h}}^{\prime}}\boldsymbol{h}_2 = c_2\boldsymbol{h}_0$, it follows that:

$$\mathbf{Y}^{\prime} = \boldsymbol{h}_0\left(a_1c_1\boldsymbol{p}_1^T + a_2c_2\boldsymbol{p}_2^T\right) \tag{26}$$

where the projection coefficients c_1 and c_2 are given by:

$$c_1 = \frac{\boldsymbol{h}_0^H\mathbf{P}_{\hat{\boldsymbol{h}}^{\prime}}\boldsymbol{h}_1}{\boldsymbol{h}_0^H\mathbf{P}_{\hat{\boldsymbol{h}}^{\prime}}\boldsymbol{h}_0}, c_2 = \frac{\boldsymbol{h}_0^H\mathbf{P}_{\hat{\boldsymbol{h}}^{\prime}}\boldsymbol{h}_2}{\boldsymbol{h}_0^H\mathbf{P}_{\hat{\boldsymbol{h}}^{\prime}}\boldsymbol{h}_0} \tag{27}$$

By defining $\delta_{ij} = \boldsymbol{h}_i^H\boldsymbol{h}_j$ as the inner product of the Jones vectors (where i,j = 0,1,2, or $\prime$), the coefficients can be simplified to:

$$c_1 = \frac{\delta_{01} - \delta_{0^{\prime}}\delta_{\prime 1}}{1 - |\delta_{0^{\prime}}|^2}, c_2 = \frac{\delta_{02} - \delta_{0^{\prime}}\delta_{\prime 2}}{1 - |\delta_{0^{\prime}}|^2} \tag{28}$$

Ultimately, the final output of the oblique projection can be expressed as:

$$\mathbf{Y}^{\prime} = \boldsymbol{h}_0\left[a_1\frac{\delta_{01} - \delta_{0^{\prime}}\delta_{\prime 1}}{1 - |\delta_{0^{\prime}}|^2}\boldsymbol{p}_1^T + a_2\frac{\delta_{02} - \delta_{0^{\prime}}\delta_{\prime 2}}{1 - |\delta_{0^{\prime}}|^2}\boldsymbol{p}_2^T\right] \tag{29}$$

In this general case, each row of the output matrix is a linear combination of the steering vectors $\boldsymbol{p}_1^T$ and $\boldsymbol{p}_2^T$. Consequently:

$$\left|\left|\frac{\mathbf{Y}'(k,:)}{\mathbf{Y}'(k,1)} - \boldsymbol{p}_0^T\right|\right| \geq 0 \tag{30}$$

The equality in Equation (30) holds if and only if:

$$a_1 c_1 \boldsymbol{p}_1^T + a_2 c_2 \boldsymbol{p}_2^T = k\boldsymbol{p}_0^T \tag{31}$$

However, the term on the left side of Equation (31) is coupled by multiple factors, including the complex envelopes a_1 and a_2, the polarization Jones vectors (which determine δ_{ij}), and the spatial steering vectors $\boldsymbol{p}_1$ and $\boldsymbol{p}_2$. Therefore, the satisfy of the equality in Equation (31) under general conditions is an event with a low probability of occurrence. The conditions under which Equation (31) holds will be discussed in the subsequent analysis regarding method limitations. Next, we verify the connection between Equation (29) and Equation (20). Assuming that the four Jones vectors involved are all real-valued and satisfy the unit-norm property, let ϑ be the angular separation between $\boldsymbol{h}_2$ and $\hat{\boldsymbol{h}}'$. Based on the property of the inner product of Jones vectors, it follows that:

$$\begin{aligned} &\delta_{01} = \delta_{10} = \cos\varepsilon, \delta_{02} = \delta_{20} = \cos(\alpha - \varepsilon) \\ &\delta_{0'} = \delta_{'0} = \cos(\alpha - \varepsilon - \vartheta), \delta_{12} = \delta_{21} = \cos\alpha \\ &\delta_{'1} = \delta_{1'} = \cos(\alpha - \vartheta), \delta_{'2} = \delta_{2'} = \cos\vartheta \end{aligned} \tag{32}$$

By substituting Equations (28) and (32) into Equation (29), we obtain:

$$\mathbf{Y}' = \boldsymbol{h}_0\left(a_1\frac{\sin(\alpha - \vartheta)}{\sin(\alpha - \varepsilon - \vartheta)}\boldsymbol{p}_1^T + a_2\frac{\sin\vartheta}{\sin(\alpha - \varepsilon - \vartheta)}\boldsymbol{p}_2^T\right) \tag{33}$$

When $\boldsymbol{h}_2$ and $\hat{\boldsymbol{h}}'$ are aligned (i.e., $\vartheta = 0$ or π), Equation (33) reduces to:

$$\mathbf{Y}' = \frac{a_1\sin(\alpha)}{\sin(\alpha - \varepsilon)}\boldsymbol{h}_0\boldsymbol{p}_1^T \tag{34}$$

This result is identical in form to Equation (20). Therefore, the scenario described by Equation (20) is a specific instance of the general formulation in Equation (29). Accordingly, the cost function $J(\eta, \kappa)$ can be defined to steer the search vector toward the true values:

$$J(\eta,\kappa) = \sum_{k=1}^{2}\left|\left|\frac{\mathbf{Y}'(k,:)}{\mathbf{Y}'(k,1)} - \mathbf{p}_0^T(\eta,\kappa)\right|\right|^2 \tag{35}$$

3.3. Implementation and 3D Imaging

Note that the aforementioned analysis is based on noise-free ideal conditions. In practice, when processing noisy echoes, the ideal condition where the norm in Equation (30) vanishes cannot be strictly satisfied, even if the search vector is perfectly aligned with the spatial steering vector of a source. However, according to Equation (33), for a given set of dual-source angles, the disparity between the rows of $\mathbf{Y}'$ and the search vector $\boldsymbol{p}_0^T$ is primarily governed by the angle ϑ, which is determined by $\hat{\boldsymbol{h}}'$. As $\hat{\boldsymbol{h}}'$ is indirectly established by the search vector $\boldsymbol{p}_0$ (via Equation (23)), this mapping mechanism ensures a smooth non-linear relationship between the cost function and the search vector, devoid

of numerical singularities. Consequently, within the 2D (η, κ) search space, the two most prominent local minima correspond to the angle estimates of the two targets, expressed as:

$$\{(\hat{\eta}_i, \hat{\kappa}_i)\}_{i=1,2} = \underset{(\eta,\kappa)}{argmin^{(2)}} J(\eta, \kappa) \tag{36}$$

where $\min^{(2)}$ denotes the selection of the two independent variables (η, κ) that yield the two smallest values of the cost function. By integrating these angular estimates with the radar ranging results R, 3D imaging (localization) of the targets can be achieved. Combined with the conversion formulas between monopulse ratios and angles (Equations (5) and (6)), the 3D Cartesian coordinates of the targets are given by:

$$\begin{cases} \hat{x}_i = R \cdot \cos\left(\frac{\hat{\eta}_i}{k_{el}} + \varphi_0\right) \sin\left(\frac{\hat{\kappa}_i}{k_{az}} + \theta_0\right) \\ \hat{y}_i = R \cdot \sin\left(\frac{\hat{\eta}_i}{k_{el}} + \varphi_0\right) \\ \hat{z}_i = R \cdot \cos\left(\frac{\hat{\eta}_i}{k_{el}} + \varphi_0\right) \cos\left(\frac{\hat{\kappa}_i}{k_{az}} + \theta_0\right) \end{cases} \tag{37}$$

3.4. Reduction in the Search Space

It has been proven that the cost function reaches its minimum if and only if the search vector is correct. However, for applications requiring high estimation precision, an exhaustive traversal of the 2D search space imposes a significant computational overhead. Therefore, we propose a search space reduction method tailored for dual-target scenarios. The core principle is that traditional monopulse estimation (the ratio of the difference channel to the sum channel) yields a "composite angle" located between the two targets. By varying the polarization reception weights, the relative energy ratio of the two sources can be altered, causing the estimated composite angles to shift within the 2D angular plane (azimuth and elevation). Theoretically, these shifted points should be collinear, lying on a straight line that connects the true angular coordinates of the two targets. Utilizing L different Jones vectors $\boldsymbol{h}^l$, a polarization projection matrix is constructed:

$$\mathbf{H} = [\boldsymbol{h}^1, \boldsymbol{h}^2, \ldots, \mathbf{h}^L] \in \mathbb{C}^{2\times L} \tag{38}$$

Applying this matrix to the original data yields:

$$\begin{aligned} \mathbf{Z} &= \mathbf{H}^H \mathbf{X}^T = a_1 \mathbf{H}^H \boldsymbol{h}_1 \boldsymbol{p}_1{}^T + a_2 \mathbf{H}^H \boldsymbol{h}_2 \boldsymbol{p}_2{}^T \\ &= [\lambda_{1,1}\boldsymbol{p}_1 + \lambda_{2,1}\boldsymbol{p}_2, \cdots, \lambda_{1,l}\boldsymbol{p}_1 + \lambda_{2,l}\boldsymbol{p}_2, \cdots, \lambda_{1,L}\boldsymbol{p}_1 + \lambda_{2,L}\boldsymbol{p}_2]^T \end{aligned} \tag{39}$$

where the coefficients $\lambda_{1,l} = a_1 \boldsymbol{h}^{lH} \boldsymbol{h}_1$ and $\lambda_{2,l} = a_2 \boldsymbol{h}^{lH} \boldsymbol{h}_2$ represent the complex envelopes after projection by the l-th random Jones vector. Direct monopulse estimation on the results in Equation (39) gives the estimated angles for each projection:

$$\begin{aligned} \hat{\eta}^l &= \frac{j\mathbf{Z}_{l,2}}{\mathbf{Z}_{l,1}} = \frac{(\lambda_{1,l}\eta_1 + \lambda_{2,l}\eta_2)}{\lambda_{1,l} + \lambda_{2,l}} \\ \hat{\kappa}^l &= \frac{j\mathbf{Z}_{l,3}}{\mathbf{Z}_{l,1}} = \frac{(\lambda_{1,l}\kappa_1 + \lambda_{2,l}\kappa_2)}{\lambda_{1,l} + \lambda_{2,l}} \end{aligned} \tag{40}$$

These can be further simplified into a linear equation in terms of $\hat{\eta}^l$ and $\hat{\kappa}^l$:

$$(\kappa_2 - \kappa_1)\hat{\eta}^l - (\eta_2 - \eta_1)\hat{\kappa}^l + j(\eta_1\kappa_2 - \eta_2\kappa_1) = 0 \tag{41}$$

This indicates that the estimation results $(\hat{\eta}^l, \hat{\kappa}^l)$ are weighted combinations of the true target points (η_1, κ_1) and (η_2, κ_2). Consequently, the L sets of coordinates calculated via Equation (40) are all located on the line defined by the actual target angles. Based on this property, we can first fit a straight line to these points and then perform the optimiza-

tion search (Equation (36)) exclusively along this line, thereby significantly reducing the computational complexity while obtaining the true angle estimates.

It should be noted that the effectiveness of this 1D reduction strategy is inherently influenced by the SNR. Under low SNR conditions, the noise term heavily perturbs the composite echoes, causing the L sets of estimated points $(\hat{\eta}^l, \hat{\kappa}^l)$ to become highly scattered. Consequently, a standard linear fit may yield a biased line that deviates from the true trajectory connecting the two targets. If the fitted search line is biased, the true target parameters will not lie exactly on the 1D search path. In such cases, the subsequent 1D search will only converge to a sub-optimal local minimum (i.e., the mathematical projection of the true minimum onto the erroneous line), ultimately introducing an inherent estimation bias and increasing the Mean Square Error (MSE). Therefore, to mitigate the influence of severe scattering and outliers in low-SNR scenarios, robust line-fitting techniques—such as Total Least Squares (TLS) [33], Orthogonal Distance Regression (ODR) [34], or the Random Sample Consensus (RANSAC) algorithm [35]—can be actively employed to secure the reliability of the spatial dimension reduction.

3.5. Analysis of Method Limitations

The proposed method primarily relies on the joint disparities in the spatial steering vectors and polarization Jones vectors to achieve dual-target discrimination. It is therefore essential to analyze how these disparities influence the estimation performance, as established by the mechanism in Equation (31). Based on the 4D orthogonal projection matrix defined in Equation (12), the steering vectors of the two targets in Equation (22) can be decomposed into a linear combination of four orthogonal basis vectors:

$$\boldsymbol{p}_i = \varsigma_i \boldsymbol{p}_0 + \alpha_i \delta_{\kappa i} \underbrace{\begin{bmatrix} -\kappa \\ 1 \\ -\eta\kappa \\ \eta \end{bmatrix}}_{\mathbf{v}_1} + \beta_i \delta_{\eta i} \underbrace{\begin{bmatrix} -\eta \\ -\eta\kappa \\ 1 \\ \kappa \end{bmatrix}}_{\mathbf{v}_2} + \delta_{\eta i}\delta_{\kappa i} \underbrace{\begin{bmatrix} \eta\kappa \\ -\eta \\ -\kappa \\ 1 \end{bmatrix}}_{\mathbf{v}_3} \tag{42}$$

where $\varsigma_i \boldsymbol{p}_0$ represents the component of the i-th target along the direction of the search vector $\boldsymbol{p}_0$. The vectors $\mathbf{v}_1$, $\mathbf{v}_2$, and $\mathbf{v}_3$ are the orthogonal basis vectors determined by $\boldsymbol{p}_0$, which collectively span the orthogonal complement of $\boldsymbol{p}_0$. The coefficients are defined as:

$$\delta\kappa_i = \frac{\kappa_i - \kappa}{1+\kappa^2}, \delta\eta_i = \frac{\eta_i - \eta}{1+\eta^2}, \alpha_i = \frac{1+\eta\eta_i}{1+\eta^2}, \beta_i = \frac{1+\kappa\kappa_i}{1+\kappa^2} \tag{43}$$

Consider the scenario where one of the angular parameters is identical for both targets. Based on the previous definition of the search space, the angular parameters of the search vector will lie on the line defined by the coordinates of the two targets. Consequently, the search parameter in that dimension will match the true parameters of the sources. For instance, in the case of identical elevation ($\eta_1 = \eta_2 = \eta_0$), the coefficient $\delta\eta_i$ vanishes and α_i becomes unity. In this situation, Equation (42) undergoes severe degeneracy:

$$\boldsymbol{p}_i = \varsigma_i \boldsymbol{p}_0 + \frac{\kappa_i - \kappa}{1+\kappa^2}\mathbf{V}_1 \tag{44}$$

The original data matrix can then be reformulated as:

$$\begin{aligned} \mathbf{X} &= a_1 \boldsymbol{p}_1 \boldsymbol{h}_1{}^T + a_2 \boldsymbol{p}_2 \boldsymbol{h}_2{}^T \\ &= \boldsymbol{p}_0 \underbrace{(\varsigma_1 a_1 \boldsymbol{h}_1{}^T + \varsigma_2 a_2 \boldsymbol{h}_2{}^T)}_{\boldsymbol{h}_A^T} + \mathbf{V}_1 \underbrace{\left(\frac{\kappa_1 - \kappa}{1+\kappa^2} a_1 \boldsymbol{h}_1{}^T + \frac{\kappa_2 - \kappa}{1+\kappa^2} a_2 \boldsymbol{h}_2{}^T\right)}_{\boldsymbol{h}_B^T} \end{aligned} \tag{45}$$

where $\boldsymbol{h}_A^T$ and $\boldsymbol{h}_B^T$ are the composite polarization vectors. The residual component obtained after performing the orthogonal projection on the data is:

$$\mathbf{X}_{\mathrm{p}} = \mathbf{P}_{\perp}\mathbf{V}_1\boldsymbol{h}_B^T \tag{46}$$

The estimated polarization steering vector at this stage is essentially the composite vector $\boldsymbol{h}_B^T$, which comprises a weighted combination of the targets' polarization states. These weights are determined by the offsets between the search parameter κ_0 and the true parameters κ_1 and κ_2. By constructing the oblique projection matrix and applying it to the original data, we obtain:

$$\begin{aligned}\mathbf{Y}' &= \mathbf{P}_{\boldsymbol{h}_0|\boldsymbol{h}_B}\mathbf{X}^T = \mathbf{P}_{\boldsymbol{h}_0|\boldsymbol{h}_B}\boldsymbol{h}_A\boldsymbol{p}_0^T + \mathbf{P}_{\boldsymbol{h}_0|\boldsymbol{h}_B}\boldsymbol{h}_B\mathbf{V}_1^T \\ &= \mathbf{P}_{\boldsymbol{h}_0|\boldsymbol{h}_B}\boldsymbol{h}_A\boldsymbol{p}_0^T + \mathbf{0} \\ &= \mathbf{P}_{\boldsymbol{h}_0|\boldsymbol{h}_B}(\varsigma_1 a_1\boldsymbol{h}_1 + \varsigma_2 a_2\boldsymbol{h}_2)\boldsymbol{p}_0^T \\ &= (\varsigma_1 a_1 c_1 + \varsigma_2 a_2 c_2)\boldsymbol{h}_0\boldsymbol{p}_0^T\end{aligned} \tag{47}$$

Consequently, the extracted spatial steering vector is identically equal to the search vector. This implies that regardless of the azimuth search parameter κ_0, each row of the output matrix will necessarily be aligned to $\boldsymbol{p}_0^T$ as long as the elevation search parameter is correct. The feedback verification thus degrades into an identity relationship, losing its capability to discriminate between different values of κ_0. A similar scenario occurs when the targets share the same azimuth angle, where the system loses its ability to distinguish η_0.

The root cause of the algorithm's failure under single-dimension angular overlap is the lack of spatial isolation, which triggers a degeneracy of the subspace orthogonal to the search vector. As derived in Equations (42)–(45), the observation signal space collapses into a second-order subspace spanned by the search vector $\boldsymbol{p}_0$ and the tangential basis vector $\mathbf{v}_1$. Since the polarization estimation stage inherently "locks onto" all energy components in the non-searched dimensions, the subsequent oblique projection forces the results to align with $\boldsymbol{p}_0$, leading to spurious search convergence. In contrast, when the residual in Equation (45) contains more than just the orthogonal component $\mathbf{v}_1$, the oblique projection matrix—designed to suppress only a single predefined polarization component—cannot simultaneously nullify the three orthogonal basis components $\mathbf{v}_1$, $\mathbf{v}_2$, and $\mathbf{v}_3$. This allows the spatial energy that deviates from the search direction $\boldsymbol{p}_0$ to be preserved, thereby guaranteeing the validity of the feedback verification step.

3.6. Performance Analysis Under Multi-Snapshot Scenarios

For fully coherent sources, the utility of multiple snapshots is typically interpreted as an effective SNR enhancement, achieved through coherent accumulation of target components and reduction in independent Gaussian noise power. However, for moving targets, the time-varying Doppler frequency often precludes lossless energy accumulation via simple Doppler filtering. In the cost function defined in Equation (35), the use of inter-channel ratios ensures that the common-mode Doppler phase φ_m (induced by temporal sampling across total M snapshots) cancels out, thereby providing a significant performance gain. This is formulated as:

$$J(\eta,\kappa) = \sum_{k=1}^{2}\left|\left|\sum_{m=1}^{M}\frac{\mathbf{Y}'_m(k,:)\exp(j\varphi_m)}{\mathbf{Y}'_m(k,1)\exp(j\varphi_m)} - \mathbf{p}_0^T(\eta,\kappa)\right|\right|^2 = \sum_{k=1}^{2}\left|\left|\sum_{m=1}^{M}\frac{\mathbf{Y}'_m(k,:)}{\mathbf{Y}'_m(k,1)} - \mathbf{p}_0^T(\eta,\kappa)\right|\right|^2 \tag{48}$$

On the other hand, based on the definition of covariance, we have:

$$\begin{aligned}&\mathrm{Cov}\left(\frac{\mathbf{Y}'(k,j)}{\mathbf{Y}'(k,1)}, \mathbf{Y}'(k,1)\right) = E\left[\frac{\mathbf{Y}'(k,j)}{\mathbf{Y}'(k,1)}\cdot\mathbf{Y}'(k,1)\right] - E\left[\frac{\mathbf{Y}'(k,j)}{\mathbf{Y}'(k,1)}\right]E[\mathbf{Y}'(k,1)] \\ &= E[\mathbf{Y}'(k,j)] - E\left[\frac{\mathbf{Y}'(k,j)}{\mathbf{Y}'(k,1)}\right]E[\mathbf{Y}'(k,1)] \quad j = 2,3,4\end{aligned} \tag{49}$$

Under the condition that $E[\mathbf{Y}'(k,1)] \neq 0$, the expectation of the ratio is given by:

$$E\left[\frac{\mathbf{Y}'(k,j)}{\mathbf{Y}'(k,1)}\right] = \frac{E[[\mathbf{Y}'(k,j)]]}{E[\mathbf{Y}'(k,1)]} - \frac{\mathrm{Cov}\left(\frac{\mathbf{Y}'(k,j)}{\mathbf{Y}'(k,1)}, \mathbf{Y}'(k,1)\right)}{E[\mathbf{Y}'(k,1)]} \tag{50}$$

It is evident that a statistical bias exists between the expectation of the ratio and the ratio of the expectations when the inter-channel ratio is correlated with the denominator (the sum channel). When the search vector differs from the true steering vector (provided the scenario does not fall into the aforementioned failure cases), the estimated Jones vector is a complex function of κ and η. Consequently, the resulting oblique projection output also becomes a function of these parameters, leading to a non-zero covariance term in Equation (50). Even when the search vector is correct, the estimated ratio is a noisy perturbation of the true monopulse ratio. Due to the presence of the shared term $\mathbf{Y}'(k,1)$ in both the numerator and denominator, this bias generally remains non-zero. Therefore, while this cost function circumvents the stringent requirement for coherent integration typically associated with multi-snapshot processing, it simultaneously introduces an inherent complexity that exerts an adverse influence on the feedback verification mechanism.

4. Experimental Results

To verify the theoretical derivations presented above, this section assesses the performance of the proposed method under a wide range of operational conditions. Specifically, a comprehensive sensitivity analysis is conducted to evaluate the algorithm's robustness with respect to varying SNRs, inter-target power ratios, spatial orientations, polarization states, relative echo phases, and snapshot counts.

To comprehensively evaluate the performance of the proposed framework, we benchmark it against three representative classical and state-of-the-art (SOTA) methods. The rationale for selecting these specific baselines is as follows: (1) The traditional four-channel closed-form solution (FCM) [31] is included as the fundamental baseline, representing classical monopulse processing capabilities. (2) The polarimetric four-channel closed-form solution (PFCM) [7] is selected as the most direct competitor. It represents the current SOTA algebraic approach that also leverages polarization diversity for dual-target resolution in four-channel architectures. (3) Finally, the Sparse Reconstruction (SR) method [20] is included to represent modern optimization-based super-resolution paradigms.

It is worth noting that classical coherent source resolution techniques, such as spatial smoothing-based MUSIC [18] and ESPRIT [19], are intentionally omitted from our performance comparisons. While these subspace-based variants are powerful in large-scale phased arrays, they face fundamental mathematical bottlenecks in the specific context of four-channel monopulse radars under single-snapshot conditions. Subspace methods inherently require a fully restored covariance matrix. However, spatial smoothing techniques rely on partitioning the array into overlapping subarrays to restore the matrix rank. The 2×2 subarray configuration of a standard four-channel radar lacks the necessary spatial degrees of freedom to construct such overlapping subarrays. Consequently, under single-snapshot conditions, their covariance matrices suffer from irreversible rank deficiency. This inherent limitation exactly underscores the motivation of this paper: providing a robust, subspace-free solution (the proposed projection-feedback framework) that is tailored for minimal-channel architectures facing severe coherent environments.

The statistical performance of each result is evaluated based on 300 independent Monte Carlo trials. The variations between trials consist solely of initial random phases between the coherent signals and additive random noise. To ensure the robustness of the conclusions, a statistical outlier rejection procedure is applied, where the 5% most extreme outliers in the

angular estimates are excluded from the analysis. By default, the snapshot number M is set to 1, and the power ratio between the two targets is set to 0 dB. Without loss of generality, the polarization parameters for the two sources are initialized as $\boldsymbol{h}_1(\xi_1, \psi_1) = (46^\circ, 46^\circ)$ and $\boldsymbol{h}_2(\xi_2, \psi_2) = (60^\circ, 0^\circ)$, while their initial relative phase difference is assumed to follow a uniform distribution over the interval $[0, 2\pi]$.

Regarding the spatial configuration, except where noted, the separation between the target and the interference in the azimuth monopulse ratio is fixed at $\Delta\kappa = \kappa_2 - \kappa_1 = 0.4$, while their elevation monopulse ratios are set to 0.2 and -0.8, respectively. As κ_2 varies, the target and interference move along two aligned trajectories within the mainlobe. To assist readers in mapping these normalized deviations to actual physical angles, we provide a concrete conversion benchmark. Assuming a representative radar system operating at a carrier frequency of 10 GHz ($\lambda = 0.03$ m) with a 256-element square array ($N_e = 16, N_a = 16$) and a broadside beam pointing direction ($\theta_0 = 0^\circ, \varphi_0 = 0^\circ$), the corresponding conversion coefficients in Equation (5) are calculated as $k_{el} = k_{az} = 4\pi$ rad^{-1}. Under this configuration, the normalized monopulse ratio interval of 0.4 corresponds to a physical angular separation of approximately 1.82°. Given that the standard 3dB beamwidth of this array is approximately 6.35°, the two targets are located deeply within the same mainlobe ($1.82^\circ \ll 6.35^\circ$), which constitutes a severely unresolved scenario for conventional techniques. Furthermore, to bridge the gap between the theoretical monopulse ratio and engineering intuition, it is instrumental to provide a physical reference for the estimation accuracy. For the 256-element array configuration described above, a monopulse ratio MSE of 0.01 is equivalent to an angular MSE of 0.208 deg^2, which corresponds to a Root Mean Square Error (RMSE) of 0.456°. Notably, this RMSE is less than one-tenth of the system's 3 dB beamwidth, providing a concrete physical scale for interpreting the high-precision performance of the proposed algorithm.

4.1. Validation of Cost Function Effectiveness

As established in the preceding analysis, a cost function was developed to validate the correctness of the search vector, with the search space restricted to a 1D line to enhance efficiency. To verify the effectiveness of this theoretical framework, the angular coordinates (in terms of monopulse ratios) for the two targets are set to $(\eta_1, \kappa_1) = (-0.8, -0.6)$ and $(\eta_2, \kappa_2) = (0.2, -0.2)$, respectively. To construct the polarization projection matrix $\mathbf{H} = [\mathbf{h}^1, \mathbf{h}^2, \ldots, \mathbf{h}^L] \in \mathbb{C}^{2\times L}$, a deterministic grid sampling strategy is employed to initialize the polarization parameters instead of random selection. Specifically, the polarization auxiliary angle $\xi \in [0, \pi/2]$ and the phase difference $\psi \in [-\pi, \pi]$ are uniformly sampled at $N_\xi = 6$ and $N_\psi = 6$ points within their respective domains, given by:

$$\begin{cases} \xi_m = \frac{(m-1)\pi}{2(N_\xi - 1)}, & m = 1, \ldots, N_\xi \\ \psi_n = -\pi + \frac{2(n-1)\pi}{N_\psi - 1}, & n = 1, \ldots, N_\psi \end{cases} \tag{51}$$

This results in a total of $L = N_\xi \times N_\psi = 36$ representative initial Jones vectors. This sampling density ensures a sufficiently uniform coverage of the Poincaré sphere, which enhances the robustness of the subsequent linear fitting process for the orientation of the line $\mathcal{L}$ in Equation (41), particularly in low signal-to-noise ratio (SNR) scenarios. Figure 3 illustrates the resulting cost function curves obtained by searching across the candidate points on the reduced 1D line. The black dots represent the true angular coordinates of the two targets in the (η, κ) domain. The lines are fitted using composite angle estimates obtained from multiple random polarization projections (Equation (41)) under different SNR conditions. The results demonstrate that the composite measurements are collinear, and the

fitted line accurately intersects the target positions at high SNRs, effectively reducing the 2D search space to a 1D candidate line.

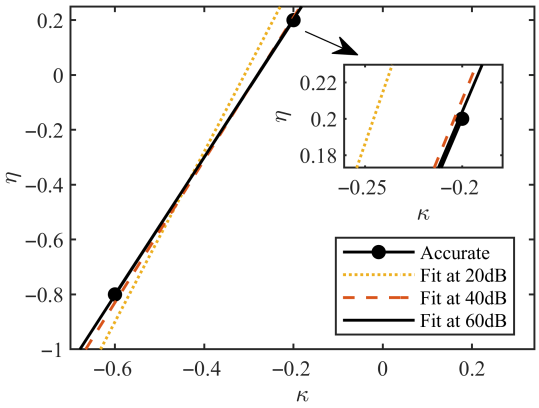

Figure 3. Verification of the search space reduction strategy. The black dots represent the true angular coordinates of the two targets at $(\eta_1, \kappa_1) = (-0.8, -0.6)$ and $(\eta_2, \kappa_2) = (0.2, -0.2)$.

To further investigate the influence of noise on the proposed verification mechanism, Figure 4 illustrates the cost function behavior evaluated along the candidate point set derived in Figure 3. Due to the linear dependency between η and κ established by the 1D fitted line, the cost function is plotted as a function of κ for a more intuitive sensitivity analysis. The black solid curve represents the performance at a high SNR of 60 dB. It is evident that two distinct global minima emerge at $\kappa_1 = -0.6$ and $\kappa_2 = -0.2$, which precisely align with the ground-truth azimuth monopulse ratios of the two targets. This confirms the algorithm's ability to achieve highly accurate parameter estimation under favorable SNR conditions. In contrast, the dashed and dotted curves indicate that decreasing SNR levels degrade the discriminative power of the cost function. At lower SNRs, the troughs of the cost function become shallower and their minima exhibit slight offsets from the true values, reflecting the expected sensitivity to noise-induced perturbations.

It is noteworthy that the proposed verification mechanism is equally applicable to single-target scenarios. As demonstrated in Figure 5, the primary distinction is that the cost function exhibits a unique global minimum instead of the dual troughs seen in multi-target cases. Consequently, the algorithm consistently provides accurate angular estimates for both single- and dual-target configurations. By integrating these estimates with range information, effective 3D imaging and localization can be achieved across diverse target environments. Existing approaches often assume a known number of targets (one or two) to apply the corresponding closed-form estimator. In contrast, our method does not require such prior assumptions, thereby improving environmental adaptability and avoiding performance degradation caused by incorrect target-count classification.

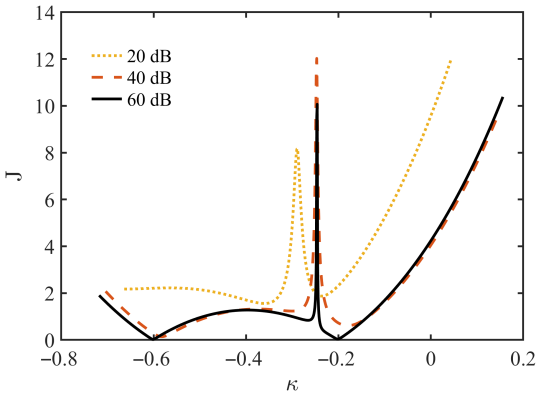

Figure 4. Cost function value under two targets. $(\eta_1, \kappa_1) = (-0.8, -0.6)$ and $(\eta_2, \kappa_2) = (0.2, -0.2)$.

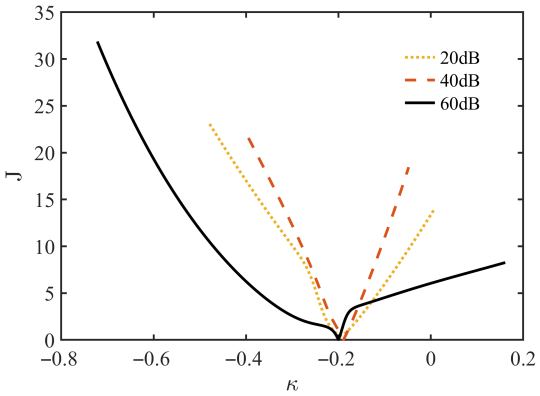

Figure 5. Cost function value under one target.

To evaluate the statistical performance of the proposed algorithm, Figure 6 presents the distribution of the estimated azimuth and elevation monopulse ratios from 300 Monte Carlo trials at an SNR of 40 dB. The clusters of black squares represent the estimated positions, which tightly surround the ground truth (red stars) for both targets. As indicated by the statistical metrics in the figure, both targets exhibit extremely low variance and bias, demonstrating the high precision of the proposed projection-feedback mechanism under high SNR. Most importantly, the blue circle represents the result of the traditional monopulse ratio (MR) method, which incorrectly provides a single "composite" angle estimate located between the two real targets. This clearly illustrates that while traditional methods fail to resolve multiple targets within the mainlobe, the proposed method successfully achieves super-resolution. The tight clustering and minimal bias further confirm the algorithm's robustness and its potential for high-fidelity 3D imaging.

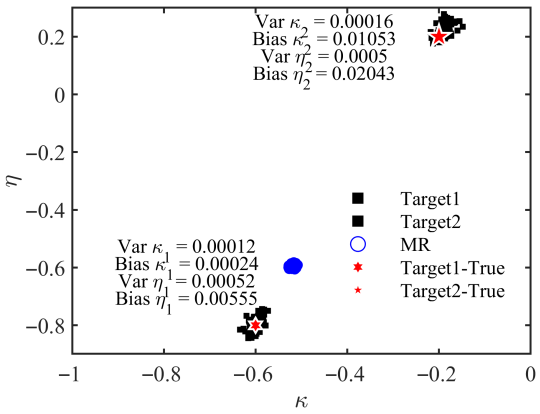

Figure 6. Angle estimation results at an SNR of 40 dB. "MR" denotes the traditional Monopulse Ratio method.

Figure 7 illustrates the 3D imaging results for five point targets by integrating the estimated 2D angles with the radar ranging information. The targets are distributed across three distinct range gates (set at specific radial distances of approximately 5.05 km, 5.00 km, and 4.95 km): R1 (Target 1 and 2), R2 (Target 3 and 4), and R3 (Target 5). A critical observation can be made at R2 range gate, where Target 3 and Target 4 are located. Due to their presence within the same range resolution cell and their coherent nature, the basic monopulse ratio method fails to resolve them. This conventional approach yields a single "Error result" (marked by the blue star) located at a certain point on the line connecting the true positions of the two sources. In contrast, the proposed method successfully resolves these coherent targets into their true spatial positions with high precision. Similar conclusions can be drawn for the R1 range gate, which further validates the consistent effectiveness and robustness of the proposed framework in achieving accurate 3D imaging

across different range bins. Finally, by mapping the 2D angular coordinates (η, κ) into the 3D Cartesian space (X, Y, Z), the accurate spatial reconstruction of all five targets is achieved, validating the potential of the proposed framework for advanced radar remote sensing and 3D surveillance applications.

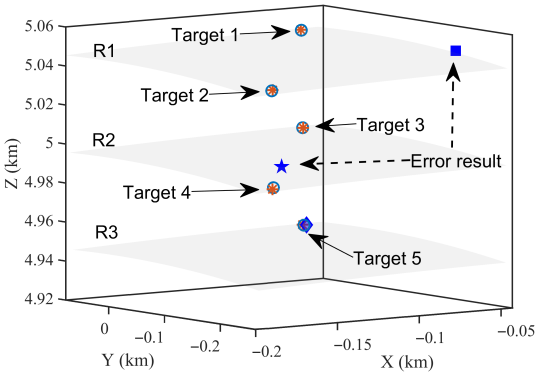

Figure 7. 3D imaging and localization results for five airborne targets across multiple range bins. The blue circles represent the true positions, and the red asterisks (*) indicate the estimation results of the proposed method.

4.2. Analysis of Factors Affecting Angle Estimation Performance

Figure 8 illustrates the MSE performance of the proposed algorithm as a function of the SNR. As expected, the MSE of the azimuth (κ) and elevation (η) estimates for both targets decreases linearly on a logarithmic scale with increasing SNR, demonstrating the statistical consistency of the proposed estimator. Specifically, under the default parameter configuration, the azimuth estimates (e.g., Tar1-azimuth) exhibit slightly higher precision than the elevation estimates. This is attributed to the sensitivity of the estimation performance to the combined effects of relative phase, angular offsets, and polarization parameters; the coupling of these factors inherently leads to non-identical estimation accuracy across the four parameters under the same SNR conditions. Even at a relatively low SNR of 30 dB (a level commonly achievable in conventional radar detection of low-altitude targets), the MSE remains approximately at the 10^{-2} level. This confirms the algorithm's capability to provide reliable angular super-resolution and high-fidelity 3D imaging of point target clusters under practical noise environments.

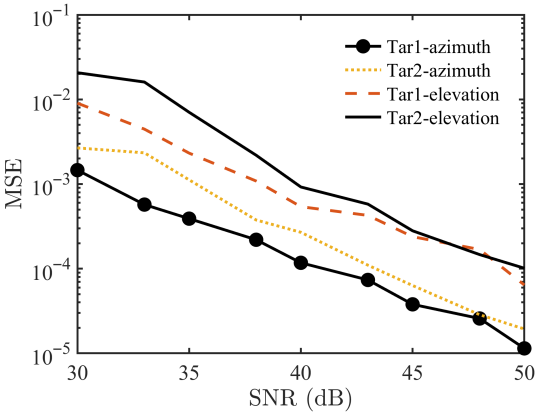

Figure 8. Statistical estimation performance in terms of MSE versus SNR.

The influence of power disparity between the two targets is further evaluated at a fixed SNR of 40 dB to assess the algorithm's robustness. Based on the power ratio defined in Equation (11), the estimation performance for the four angular parameters is recorded as the γ increases from 0 dB to 30 dB. As illustrated in Figure 9, the MSE for Target 1 (both

azimuth and elevation) decreases significantly with the rising γ, a trend consistent with the increased individual signal energy of that source. Crucially, the estimation accuracy for Target 2 remains remarkably stable across the entire 30 dB power range. This phenomenon highlights the robust decoupling capability of the proposed projection-feedback mechanism, which effectively mitigates the "masking effect" where a dominant source obscures its weaker neighbor. Specifically, the oblique projection effectively suppresses the energy leakage from the stronger target into the estimation process of the weaker one. Such performance is of vital importance for practical radar surveillance scenarios where targets with diverse radar cross-sections (RCSs) coexist within the same mainlobe.

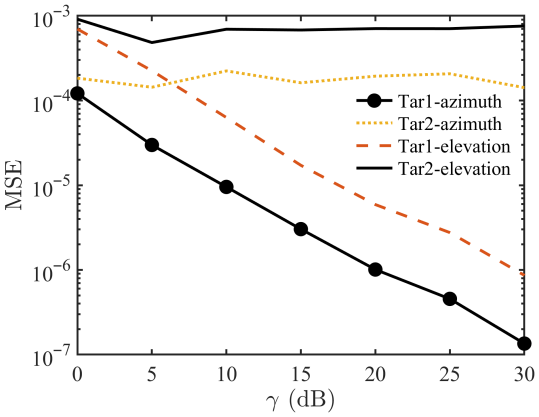

Figure 9. Statistical estimation performance in terms of MSE versus power ratio.

To further investigate the inter-target interaction, Figure 10 illustrates the impact of azimuth and elevation separations on the estimation accuracy. To quantify the overall estimation accuracy, we utilize the 'Total MSE', which represents the sum of the individual mean square errors for Target 1 and Target 2 within a specific angular dimension (e.g., the total azimuth MSE is the sum of the individual azimuth MSEs for the two targets). A key observation is the cross-dimensional performance enhancement: as the angular separation in one dimension (e.g., azimuth $\Delta\kappa$) increases, the estimation precision in the orthogonal dimension (e.g., elevation η) improves significantly. Conversely, the relationship between angular separation and accuracy within the same dimension does not exhibit such a monotonic trend and appears more complex. This phenomenon aligns with the theoretical limitation analysis provided in Section 3.5. When two coherent sources overlap in one dimension, the lack of spatial isolation leads to subspace degeneracy, which fundamentally causes the estimation in the orthogonal dimension to fail. However, the intra-dimensional estimation accuracy is governed not only by the correlation of the spatial steering vectors but also by the specific absolute values of the parameters. This observation is consistent with the Cramer–Rao Lower Bound (CRLB) analysis for multi-target monopulse radars presented in [7], which suggests that cross-dimensional coupling is an inherent characteristic of the sum-and-difference architecture.

4.3. Comparative Superiority over Existing Methods

4.3.1. Robustness to Relative Phase Difference

For coherent sources, the disparity between time-domain echo signals is primarily manifested in their initial relative phases. Figure 11 presents a performance comparison between the proposed method and the four-channel closed-form solution from Literature [31] across a range of phase differences. Since the proposed processing framework hinges entirely on the disparities in spatial steering vectors and polarization Jones vectors, it remains inherently independent of waveform parameters. Consequently, the MSE curves of the proposed method remain remarkably flat across the entire phase range. In traditional

coherent source estimation, performance often degrades significantly at specific "sensitive phases". The results here demonstrate that the proposed projection-feedback mechanism is immune to phase variations. This stability is a significant advantage for practical radar applications, as it ensures reliable super-resolution and imaging performance regardless of the random phase relationships between targets.

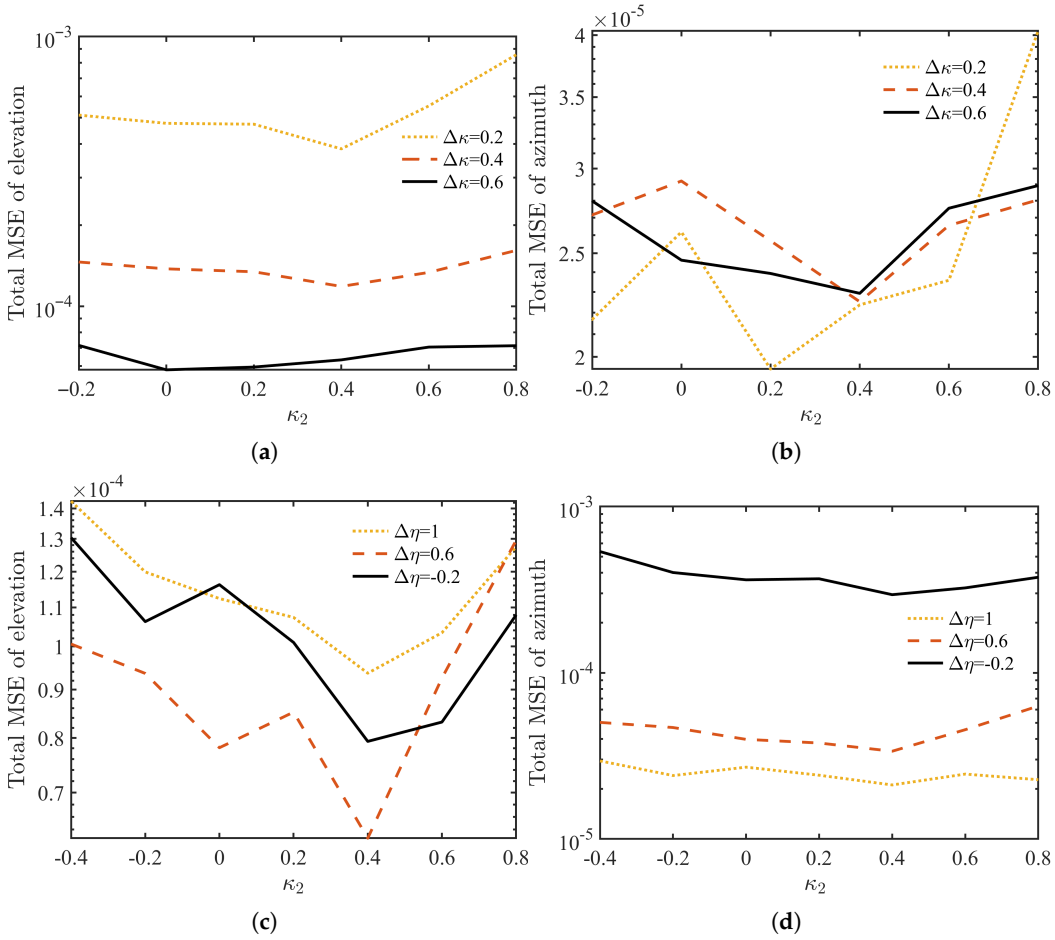

Figure 10. Impact of angular separations on the estimation performance (Total MSE) in azimuth and elevation at a fixed SNR of 50 dB. (**a**) $\Delta\kappa$ on total MSE of η. (**b**) $\Delta\kappa$ on total MSE of κ. (**c**) $\Delta\eta$ on total MSE of η. (**d**) $\Delta\eta$ on total MSE of κ.

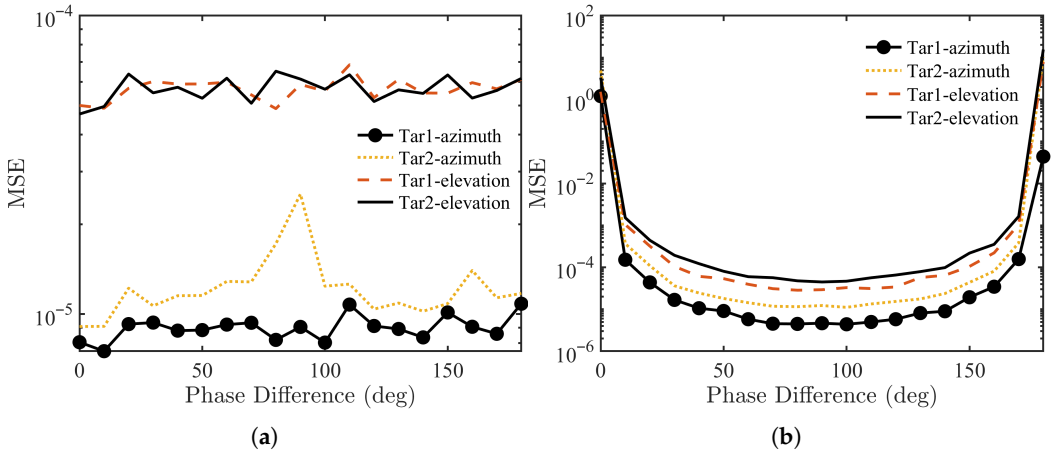

Figure 11. Performance comparison of angle estimation accuracy versus relative phase difference at a fixed SNR of 50 dB. (**a**) Performance of the proposed method. (**b**) Performance of the four-channel closed-form solution from [31].

4.3.2. Improved Performance Under Small Polarization Disparity

The proposed method is built upon the joint diversity of polarization and spatial domains. Similarly, Literature [7] leverages these diversities for single-snapshot angle estimation of dual targets, with its core principle being adaptive polarization nulling to suppress one signal component before estimating the parameters of the other. Figure 12 compares the angular estimation performance of three methods in scenarios characterized by high polarization similarity. In this scenario, the Jones vectors for the two sources are initialized as $\boldsymbol{h}_1(\xi_1, \psi_1) = (45°, 0°)$ and $\boldsymbol{h}_2(\xi_2, \psi_2) = (\xi, 0°)$, respectively. The SNR is set to 40 dB.Furthermore, the total MSE for a specific target is redefined as the sum of the mean square errors of its estimated azimuth and elevation parameters.

As illustrated in Figure 12, A prominent performance singularity (MSE peak) is observed at 45°, where the polarization states of the two targets become identical. This phenomenon confirms the theoretical expectation that when polarization diversity vanishes, the "blind zone" of the spatial-polarization framework is triggered, leading to estimation failure. However, in the regions where polarization states are distinguishable, the proposed method (dotted line) consistently demonstrates superior precision. As highlighted in the magnified insets, the MSE of the proposed approach is lower than that of the PFCM (dashed line), validating that our refined projection-feedback mechanism provides enhanced accuracy even under high polarization similarity.

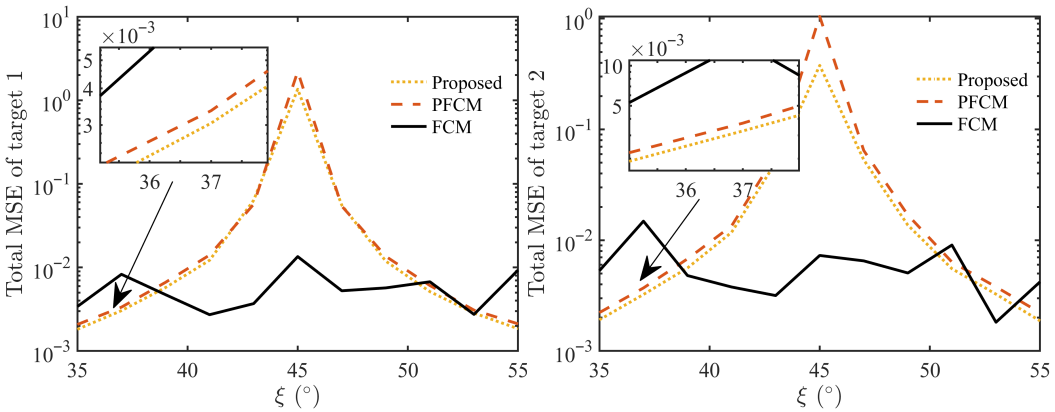

Figure 12. Angular estimation performance comparison under varying polarization relationship angles at a fixed SNR of 40 dB. (**a**) Total MSE of Target 1. (**b**) Total MSE of Target 2.

4.3.3. Improved Performance Under Multi-Snapshot Processing

The performance gain derived from multi-snapshot processing is further investigated by varying the number of snapshots M from 8 to 32. It is imperative to emphasize that the core projection-feedback framework proposed in this paper is fundamentally designed to operate strictly on single-snapshot data. The multi-snapshot processing discussed in this section is not an algorithmic prerequisite for resolving coherent targets. Rather, it serves as an optional extension to harness effective SNR gain. Additionally, the inter-snapshot phase difference caused by Doppler estimation inaccuracy is set to fluctuate between 5° and 15°. To provide a theoretical baseline, we include "SNR-equivalent" benchmarks (Proposed-SNR and PFCM-SNR), which simulate a single-snapshot case with a power boost corresponding to the coherent integration gain of M samples ($\mathrm{SNR}_{\mathrm{equiv}} = \mathrm{SNR}_{\mathrm{single}} + 10\log_{10} M$).

As illustrated in Figure 13, under the $\mathrm{SNR}_{\mathrm{single}}$ of 30 dB, the proposed method (yellow curve) demonstrates a consistent reduction in MSE as M increases, closely following the trend of the theoretical Proposed-SNR benchmark (black solid dots). In contrast, the PFCM algorithm (dashed black line) exhibits significant instability and fails to converge

in this coherent multi-snapshot scenario, highlighting the robustness of our projection-feedback framework.

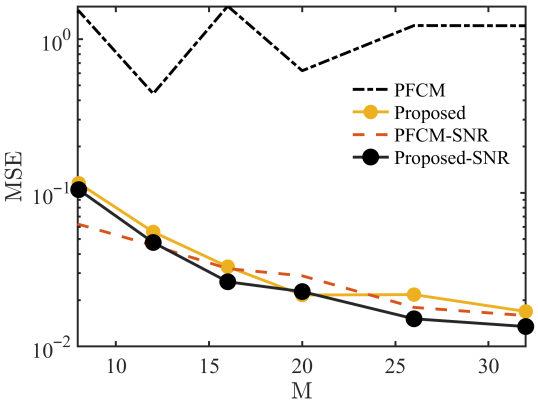

Figure 13. Comparison of angle estimation performance versus the number of snapshots M.

Notably, a marginal performance gap exists between the actual multi-snapshot results and their SNR-equivalent counterparts. While the Proposed-SNR curves represent an idealized coherent summation of signal power, the actual multi-snapshot estimation involves the non-linear averaging of monopulse ratios across M samples. As analyzed in Section 3.6, the non-linear nature of the ratio operator introduces a slight statistical bias in the presence of noise, which prevents the multi-snapshot MSE from perfectly reaching the theoretical single-snapshot SNR-gain limit. Nevertheless, the proposed method effectively harnesses the integration gain, achieving high-precision estimation that significantly outperforms traditional closed-form alternatives in complex coherent environments.

4.3.4. 3D Imaging Results for Point Target Clusters

To evaluate the comparative advantages of the proposed framework, Figure 14 illustrates the 3D imaging performance of several representative methods. The simulations are conducted using 8 snapshots at an SNR of 20 dB. Target 1's polarization parameters remain consistent with those in Figure 12, while Target 2's parameters are set to $\boldsymbol{h}_2(\xi_2, \psi_2) = (51^\circ, 0^\circ)$. Notably, the shaded regions in the figure roughly correspond to the ground-truth coordinate ranges of the targets at each distance, thereby facilitating a more intuitive comparison of the 3D imaging performance among different methods. While Doppler processing via FFT is a standard technique for coherent integration, its efficacy is fundamentally constrained by the Doppler resolution limit. In high-dynamic scenarios or short-dwell observations, insufficient resolution leads to energy smearing and scalloping loss, which significantly degrade the integration gain. Consequently, the 3D imaging results obtained by the PFCM method in Figure 14a exhibit noticeable deviations from the ground-truth target positions. The localization performance of the SR approach is presented in Figure 14b. Due to the limited number of spatial channels and high polarization similarity, the SR method struggles to accurately recover the angular and polarization weights of multiple targets using an over-complete dictionary. This mismatch often leads to substantial angular estimation errors, thereby compromising the final 3D imaging quality. In contrast, the 3D imaging results of the proposed method in Figure 14c are in much closer agreement with the actual target coordinates. This superior performance validates that the proposed projection-feedback mechanism effectively overcomes the limitations of both conventional Doppler-based integration and dictionary-based sparse recovery in complex coherent environments, maintaining high fidelity even with a restricted number of samples.

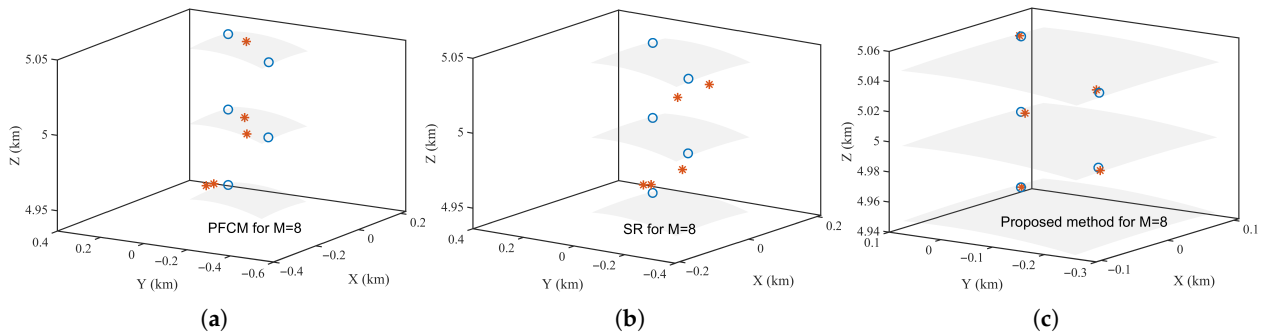

Figure 14. Comparative 3D imaging results for point target clusters using different estimation frameworks. (**a**) Results obtained via the PFCM method. (**b**) Results obtained via the SR method. (**c**) Results obtained via the proposed projection-feedback method. The blue circles represent the true positions, and the red asterisks (*) indicate the estimation results of the proposed method.

4.3.5. Computational Complexity and Execution Time Analysis

To evaluate the computational efficiency of the proposed framework, an execution time comparison was conducted. Given that the proposed method relies on a spatial search mechanism, it is benchmarked against the SR method and the standard MUSIC algorithm.

As discussed at the beginning of Section 4, the MUSIC algorithm suffers from covariance matrix rank deficiency in single-snapshot, four-channel coherent scenarios and fails to resolve the targets. However, it is deliberately included in this specific test solely to serve as a baseline for the computational overhead of a traditional 2D spatial grid search. To ensure a fair comparison of the inherent algorithmic complexity, all methods were implemented using sequential (single-threaded) processing without any parallel computing acceleration. The simulations were performed on a computer equipped with a 12th Gen Intel(R) Core(TM) i9-12900H processor.

As demonstrated in Table 1, the proposed method significantly outperforms both the SR and MUSIC algorithms in terms of computational speed. It should be noted that the search step size for each parameter was set to 0.001 for both the proposed method and the MUSIC algorithm, while the parameter interval for the dictionary atoms in the SR method was set to 0.05. The high execution time of the SR method is attributed to the iterative optimization required for sparse recovery based on an over-complete dictionary. Furthermore, compared to the traditional 2D grid search (represented by the MUSIC), the proposed method benefits tremendously from the search space reduction strategy. By leveraging polarization-angle coupling to transform the complex 2D parameter search into an efficient 1D line search, the proposed framework dramatically reduces the computational burden by over two orders of magnitude, making it highly suitable for real-time 3D radar imaging and high-dynamic tracking applications.

Table 1. Execution time comparison of different methods.

Method	Search Space Dimension	Execution Time (s)
Proposed Method	1D Line Search	0.1606
SR Method	Dictionary Optimization	45.9431
MUSIC	2D Grid Search	50.1120

4.3.6. Robustness to Hardware Imperfections

In practical radar systems, non-ideal hardware characteristics such as channel amplitude/phase mismatches and cross-polarization leakage are inevitable. Since severe hardware errors fundamentally distort the spatial steering vectors, standard calibration pro-

cedures are typically applied prior to angle estimation. Therefore, to evaluate the practical robustness of the proposed framework, we investigate its performance under the condition of post-calibration residual errors.

We conducted Monte Carlo simulations at an SNR of 40 dB, introducing equivalent sum-channel residual amplitude errors (up to 5%) and phase errors (up to 5°). As shown in Table 2, we analyzed the measurement accuracy of the monopulse ratios in the 2D angular domain (i.e., azimuth and elevation) for both Target 1 and Target 2 under various error conditions. The results indicate that while the estimation MSE of all methods degrades slightly as the residual errors increase, the proposed method achieves higher accuracy in most cases. Even under the worst-case scenario (5% amplitude error and 5° phase error), the proposed method maintains an MSE on the order of 10^{-4}, demonstrating strong robustness and significantly outperforming the PFCM and FCM algorithms.

Table 2. MSE Performance under Residual Amplitude and Phase Errors ($M = 1$).

Error Condition	Method	Tar1 Elev MSE	Tar1 Azi MSE	Tar2 Elev MSE	Tar2 Azi MSE
Ideal (Amp 0%, Phase 0°)	Proposed	$\mathbf{5.92 \times 10^{-4}}$	$\mathbf{9.84 \times 10^{-5}}$	$\mathbf{5.78 \times 10^{-4}}$	$\mathbf{1.23 \times 10^{-4}}$
	PFCM	7.57×10^{-4}	1.03×10^{-4}	6.62×10^{-4}	1.45×10^{-4}
	FCM	1.45×10^{-4}	2.69×10^{-3}	1.52×10^{-3}	4.80×10^{-3}
Phase Error Only (Amp 0%, Phase 5°)	Proposed	$\mathbf{7.27 \times 10^{-4}}$	$\mathbf{1.15 \times 10^{-4}}$	$\mathbf{7.40 \times 10^{-4}}$	2.75×10^{-4}
	PFCM	7.90×10^{-4}	1.32×10^{-4}	7.84×10^{-4}	$\mathbf{1.90 \times 10^{-4}}$
	FCM	8.20×10^{-3}	5.81×10^{-4}	5.62×10^{-3}	1.88×10^{-3}
Amplitude Error Only (Amp 5%, Phase 0°)	Proposed	$\mathbf{6.15 \times 10^{-4}}$	$\mathbf{6.92 \times 10^{-5}}$	$\mathbf{7.42 \times 10^{-4}}$	$\mathbf{2.31 \times 10^{-4}}$
	PFCM	6.96×10^{-4}	1.02×10^{-4}	8.22×10^{-4}	2.42×10^{-4}
	FCM	1.61×10^{-3}	4.06×10^{-4}	3.06×10^{-3}	6.16×10^{-4}
Combined Errors (Amp 5%, Phase 5°)	Proposed	$\mathbf{6.66 \times 10^{-4}}$	$\mathbf{1.00 \times 10^{-4}}$	9.29×10^{-4}	2.54×10^{-4}
	PFCM	8.17×10^{-4}	1.08×10^{-4}	$\mathbf{8.19 \times 10^{-4}}$	$\mathbf{2.12 \times 10^{-4}}$
	FCM	4.84×10^{-3}	8.98×10^{-4}	4.87×10^{-3}	2.42×10^{-3}

Note: Bold values indicate the best performance.

Furthermore, Table 3 illustrates the impact of cross-polarization leakage. Theoretically, both the proposed method and the PFCM utilize polarization primarily as a distinguishing feature to resolve the two coherent targets. Cross-polarization essentially causes the received polarization states to slightly deviate from the targets' true states. However, as long as the cross-polarization leakage does not cause the "observed" polarization states of the two targets to become indistinguishable, the algorithm's performance will not experience significant degradation.

From a theoretical perspective regarding the feedback mechanism, Equation (31) establishes a highly restrictive mathematical condition under which a false minimum could potentially occur during the parameter search. As analyzed in Section 3.2, satisfying this equality under non-target-aligned conditions requires an exact, coincidental coupling of complex envelopes, polarization states, and spatial vectors, making it a low-probability event even in ideal scenarios. When non-ideal hardware characteristics, such as channel imbalances and cross-polarization leakage, are introduced, they essentially act as complex perturbations to the signal parameters. Rather than facilitating this strict equality, these unpredictable hardware errors make the accidental alignment required by Equation (31) even more improbable. Consequently, these non-ideal factors do not undermine the verification mechanism by creating false minima. While the hardware perturbations cause slight deviations in the spatial locations of the true target minima, they do not cause catastrophic failure, thereby ensuring the robustness of the proposed framework.

The simulation results with 20 dB isolation and various phase rotations confirm this analysis. Although the cross-dimensional coupling leads to estimation results that deviate from the noise-only ideal case, the proposed projection-feedback mechanism effectively maintains high-precision angle measurement, securing precision over traditional closed-form alternatives in complex, non-ideal environments.

Table 3. MSE Performance under Cross-Polarization Leakage ($M = 1$).

Cross-Pol Condition	Method	Tar1 Elev MSE	Tar1 Azi MSE	Tar2 Elev MSE	Tar2 Azi MSE
Ideal (No Cross-Pol)	Proposed	$\mathbf{5.92 \times 10^{-4}}$	$\mathbf{9.84 \times 10^{-5}}$	$\mathbf{5.78 \times 10^{-4}}$	$\mathbf{1.23 \times 10^{-4}}$
	PFCM	7.57×10^{-4}	1.03×10^{-4}	6.62×10^{-4}	1.45×10^{-4}
	FCM	1.45×10^{-4}	2.69×10^{-3}	1.52×10^{-3}	4.80×10^{-3}
20 dB Isolation 30° Phase Rotation	Proposed	$\mathbf{5.52 \times 10^{-4}}$	$\mathbf{8.94 \times 10^{-5}}$	$\mathbf{5.34 \times 10^{-4}}$	$\mathbf{1.05 \times 10^{-4}}$
	PFCM	7.30×10^{-4}	1.08×10^{-4}	5.64×10^{-4}	1.05×10^{-4}
	FCM	1.63×10^{-3}	2.26×10^{-4}	2.71×10^{-3}	6.62×10^{-4}
20 dB Isolation 0° Phase Rotation	Proposed	$\mathbf{6.65 \times 10^{-4}}$	$\mathbf{8.66 \times 10^{-5}}$	$\mathbf{5.68 \times 10^{-4}}$	$\mathbf{1.40 \times 10^{-4}}$
	PFCM	7.78×10^{-4}	1.33×10^{-4}	5.89×10^{-4}	1.81×10^{-4}
	FCM	1.32×10^{-3}	3.45×10^{-4}	2.77×10^{-3}	3.87×10^{-4}

Note: Bold values indicate the best performance.

5. Conclusions

This study establishes a unified 3D imaging framework for point target clusters based on four-channel monopulse radar. A primary contribution of this work is the development of an estimation mechanism that is agnostic to target cardinality, offering broader operational applicability than conventional closed-form solutions that rely on predefined target counts.

Extensive numerical simulations under single-snapshot conditions demonstrate the proposed framework's robustness against various non-ideal factors. Notably, the method maintains high-precision angle measurement even in the presence of hardware imperfections (e.g., residual amplitude and phase errors) and cross-polarization leakage. Furthermore, it provides better performance than existing techniques in demanding scenarios characterized by arbitrary initial relative phase differences and high polarization similarities between coherent targets.

Beyond its single-snapshot capabilities, the proposed framework also exhibits outstanding performance in highly dynamic environments. Even in scenarios where short-term observations preclude full coherent integration gain, our method efficiently harnesses multi-snapshot data to achieve estimation fidelity nearly identical to that of full energy accumulation. To further refine this technology, future research will concentrate on extending the proposed framework to the angle estimation of multiple targets within a single range bin, aiming to enhance the reliability of mainlobe super-resolution in increasingly complex surveillance contexts.

Author Contributions: Conceptualization, J.T. and Z.W.; methodology, J.T.; software, J.T. and J.Z.; validation, J.T. and Z.W. ; formal analysis, J.T.; investigation, J.T. and Z.W. ; resources, Z.S. and Z.W.; data curation, J.T.; writing—original draft preparation, X.W.; writing—review and editing, Z.W., Z.S. and J.Z.; visualization, F.W.; supervision, Z.W., Z.S. and P.W.; project administration, Z.W., Z.S. and P.W.; funding acquisition, Z.W., J.Z. and P.W. All authors have read and agreed to the published version of the manuscript.

Funding: This research was funded by the National Natural Science Foundation of China under Grant 62301580 and in part by the Hunan Provincial Science and Technology Innovation Program under Grant 2024RC3138.

Data Availability Statement: The data supporting the findings of this study are generated through numerical simulations and are available from the corresponding author upon reasonable request.

Conflicts of Interest: The authors declare no conflicts of interest.

References

1. Wen, L.; Ke, M.; Jiang, M.; Ding, J.; Huang, X. Shadow Spatiotemporal Track-Before-Detect Approach for Distributed UAV-Borne Video SAR. *Remote Sens.* **2026**, *18*, 343. [CrossRef]
2. Peng, M.; Xue, J.; Xia, Z.; Du, J.; Quan, Y. A Novel Decomposition-Prediction Framework for Predicting InSAR-Derived Ground Displacement: A Case Study of the XMLC Landslide in China. *Remote Sens.* **2026**, *18*, 425. [CrossRef]
3. Chen, Y.; Shen, Y.; Duan, C.; Wang, Z.; Mo, Z.; Liang, Y.; Zhang, Q. Robust and Efficient SAR Ship Detection: An Integrated Despeckling and Detection Framework. *Remote Sens.* **2025**, *17*, 580.
4. Fu, M.; Zhang, W.; Quan, X.; Shi, D.; Tan, L.; Zhang, J.; Xing, Y.; Zhang, S. Modulation and Perturbation in Frequency Domain for SAR Ship Detection. *Remote Sens.* **2026**, *18*, 338. [CrossRef]
5. Sun, Z.; Zhang, X.; Leng, X.; Wu, X.; Xiong, B.; Ji, K.; Kuang, G. KFIA-Net: A knowledge fusion and imbalance-aware network for multi-category SAR ship detection. *Int. J. Appl. Earth Obs. Geoinf.* **2026**, *146*, 105127. [CrossRef]
6. Tian, J.; Zhou, J.; Zhou, K.; Lan, Y. Thinned array anti-jamming angle measurement technology based on oblique projection. In Proceedings of the IET International Radar Conference (IRC 2023), Chongqing, China, 3–5 December 2023.
7. Liu, Y.; Wang, S.; Wu, G.; Wang, P.; Li, Y. Robust and Unambiguous Four-Channel Monopulse Two-Target Resolution: A Polarimetric Closed-Form Approach. *IEEE Trans. Signal Process.* **2024**, *72*, 4222–4236. [CrossRef]
8. Liu, Y.; Wang, S.; Wu, G.; Wu, Z.; Wang, P.; Li, Y. Adaptive Polarization Modulation for Subarray-Based Monopulse Radar Angular Superresolution. *IEEE Trans. Aerosp. Electron. Syst.* **2025**, *61*, 14262–14275. [CrossRef]
9. Wang, W.; Zhang, L. DOA Estimation for Coherent and Non-Coherent Mixed Signals Using Toeplitz Diagonal Diffusion. *IEEE Signal Process. Lett.* **2025**, *32*, 1985–1989. [CrossRef]
10. Wang, J.Z.; Sinha, A.; Willett, P.; Bar-Shalom, Y. Angle estimation for two unresolved targets with monopulse radar. *IEEE Trans. Aerosp. Electron. Syst.* **2004**, *40*, 998–1019. [CrossRef]
11. Sinha, A.; Kirubarajan, T.; Bar-Shalom, Y. Maximum likelihood angle extractor for two closely spaced targets. *IEEE Trans. Aerosp. Electron. Syst.* **2002**, *38*, 183–203. [CrossRef]
12. Blair, W.D.; Pearce, M. Monopulse DOA Estimation of Two Unresolved Rayleigh Targets. *IEEE Trans. Aerosp. Electron. Syst.* **2002**, *37*, 452–469.
13. Schmidt, R. Multiple emitter location and signal parameter estimation. *IEEE Trans. Antennas Propag.* **1986**, *34*, 276–280. [CrossRef]
14. Liu, Z.; Wu, J.; Yang, S.; Lu, W. DOA Estimation Method Based on EMD and MUSIC for Mutual Interference in FMCW Automotive Radars. *IEEE Geosci. Remote Sens. Lett.* **2022**, *19*, 3504005 . [CrossRef]
15. Cao, J.; Yang, Z.; Chen, X. Compressed Line Spectral Estimation Using Covariance: A Sparse Reconstruction Perspective. *IEEE Signal Process. Lett.* **2024**, *31*, 2540–2544. [CrossRef]
16. Karimi, M.; Zare, M.; Derakhtian, M. Sparse Bayesian Learning with Jeffreys' Noninformative Prior for Off-Grid DOA Estimation. *Signal Process.* **2025**, *230*, 109809. [CrossRef]
17. Liu, S.; Mao, Z.; Liu, Y.; Fei, T.; Gardill, M.; Huang, Y. TRANM: Decoherenced DoA estimation for automotive radar using generalized sparse arrays. *Signal Process.* **2025**, *231*, 109744. [CrossRef]
18. Wei, J.Q.; Xu, X.; Luo, D.W.; Ye, Z.F. Sequential DOA estimation method for multi-group coherent signals. *Signal Process.* **2017**, *130*, 169–174. [CrossRef]
19. Pan, J.; Sun, M.; Wang, Y.; Zhang, X. An Enhanced Spatial Smoothing Technique With ESPRIT Algorithm for Direction of Arrival Estimation in Coherent Scenarios. *IEEE Trans. Signal Process.* **2020**, *68*, 3635–3643. [CrossRef]
20. Mecklenbräuker, C.F.; Gerstoft, P.; Ollila, E.; Park, Y. Robust and sparse M-estimation of DOA. *Signal Process.* **2024**, *220*, 109461. [CrossRef]
21. Yu, K.B.; Murrow, D.J. Adaptive digital beamforming for angle estimation in jamming. *IEEE Trans. Aerosp. Electron. Syst.* **2001**, *37*, 508–523. [CrossRef]
22. Chen, X.; Shu, T.; Yu, K.B.; Yu, W. Enhanced ADBF Architecture for Monopulse Angle Estimation in Multiple Jammings. *IEEE Antennas Wirel. Propag. Lett.* **2024**, *16*, 2684–2687. [CrossRef]
23. Wu, H.; Liu, R.; Guo, Y.; Zhang, J.; He, F.; Meng, J. Performance Analysis of Mainlobe Canceller for Monopulse At Subarray Level in the Presence of Amplitude-Phase Error. *IEEE Trans. Aerosp. Electron. Syst.* **2024**, *60*, 2461–2473. [CrossRef]
24. Yang, X.; Zhang, Z.; Zeng, T.; Long, T.; Sarkar, T.K. Mainlobe Interference Suppression Based on Eigen-Projection Processing and Covariance Matrix Reconstruction. *IEEE Antennas Wirel. Propag. Lett.* **2014**, *13*, 1369–1372. [CrossRef]

25. Zhang, M.; Song, R.; Zhang, X.; Zhang, Z.; Song, W. Main lobe jamming suppression algorithm based on blocking matrix pre-processing and covariance matrix reconstruction. In Proceedings of the 11th International Conference on Signal Processing Systems, Chengdu, China, 15–17 November 2019; Volume 11371.
26. Meng, H.; Qu, X.; Zhang, X.; Li, W.; Zhang, Z.; Yang, X. Mainlobe Interference Suppression Method Based on Blocking Matrix Preprocessing with Low Sidelobe Constraint. In Proceedings of the Asia-Pacific Signal and Information Processing Association Annual Summit and Conference (APSIPA ASC), Chiang Mai, Thailand, 7–10 November 2022; pp. 2065–2070.
27. Ge, M.; Cui, G.; Yu, X.; Kong, L. Main lobe jamming suppression via blind source separation sparse signal recovery with subarray configuration. *IET Radar Sonar Navig.* **2020**, *14*, 431–438. [CrossRef]
28. Han, X.; He, H.; Zhang, Q.; Yang, L.; He, Y.; Li, Z. Main-Lobe Jamming Suppression Method for Phased Array Netted Radar Based on MSNR-BSS. *IEEE Sens. J.* **2022**, *22*, 22972–22984. [CrossRef]
29. Tian, J.; Wang, Z.; Zhou, J.; Wang, F.; Song, Z.; Pang, C.; Wang, P. Angle estimation of a second target in monopulse radar via separation-confirmation method given the DOA of the other target. *IEEE TechRxiv* 2025, *preprint*. [CrossRef]
30. Ma, J.; Lu, D.; Liu, J.; Shi, L. A Cross-Eye Jamming Mitigation Approach for Polarized Monopulse Radars. *IEEE Trans. Aerosp. Electron. Syst.* **2025**, *61*, 5495–5498. [CrossRef]
31. Zheng, Y.; Tseng, S M.; Yu, K.B. Closed-form four-channel monopulse two-target resolution. *IEEE Trans. Aerosp. Electron. Syst.* **2003**, *39*, 1083–1089. [CrossRef]
32. Liu, X.; Wang, G.; Wang, S.; Xu, Z. Detection for unresolved targets by using complex monopulse ratio on planar array radar. *J. Natl. Univ. Def. Technol.* **2018**, *40*, 76.
33. Shi, H.; Zhang, X.; Gao, Y.; Wang, S.; Ning, Y. Robust Total Least Squares Estimation Method for Uncertain Linear Regression Model. *Mathematics* **2023**, *20*, 4354. [CrossRef]
34. Keleş, T.; Altun, M. Comparison of Classical Linear Regression and Orthogonal Regression According to the Sum of Squares Perpendicular Distances. *J. Meas. Eval. Educ. Psychol.* **2016**, *2*, 296–308.
35. Tong, Y.; Wang, Z.; Yu, Y.; Chen, Y.; Wan, C.; Zhou, X.; Tang, Y.; Kong, D. A Linear Fitting Algorithm Based on Locality Sensitive Hashing with Random Sample Consensus for the Thickness Measurement of Reconstituted Tobacco. In Proceedings of the 2024 4th International Conference on Electronic Information Engineering and Computer Science (EIECS), Yanji, China, 27–29 September 2024.

Disclaimer/Publisher's Note: The statements, opinions and data contained in all publications are solely those of the individual author(s) and contributor(s) and not of MDPI and/or the editor(s). MDPI and/or the editor(s) disclaim responsibility for any injury to people or property resulting from any ideas, methods, instructions or products referred to in the content.